



Single-atom co sites confined in layered double hydroxide for selective generation of surface-bound radicals via peroxyomonosulfate activation

Chaofa Chen ^{a,1}, Minjia Yan ^{a,1}, Yu Li ^a, Yuwen Hu ^a, Jianrong Chen ^a, Shaobin Wang ^b, Xi-Lin Wu ^{a,b,*}, Xiaoguang Duan ^{b,**}

^a College of Geography and Environmental Science, Zhejiang Normal University, Jinhua 321004, China

^b School of Chemical Engineering, The University of Adelaide, Adelaide, SA 5005, Australia



ARTICLE INFO

Keywords:

Single atom catalysts
Layered double hydroxides
Peroxyomonosulfate
Long-lived radicals
Emerging organic contaminants

ABSTRACT

Selective production of specific radical species with prolonged lifetime is challenging in advanced oxidation process. Herein, we constructed single-atom Co (SA-Co) catalytic sites confined in layered double hydroxide (LDH) for selectively and sustainably generate radical species via peroxyomonosulfate (PMS) activation. The negatively charged PMS was stabilized by the positively charged LDH and simultaneously activated by the nanoconfined Co single-atom sites, resulting in oriented-production of surface-bonded •OH and SO₄^{•-} radicals with long-term efficiency (up to 48 h), suppressed PMS decomposition and radical self-quenching. Ion competition experiments and in-situ spectroscopic studies were applied to monitor the PMS activation processes. The SA-Co-LDH/PMS system outperforms the benchmark homogeneous (Co²⁺/PMS) and heterogeneous (Co₃O₄/PMS) catalytic systems for the degradation of emerging organic contaminants (EOCs) with the lowest Co consumption and highest catalytic efficiency.

1. Introduction

Peroxyomonosulfate (PMS)-based advanced oxidation processes (AOPs) have been studied extensively for the treatment of emerging organic contaminants (EOCs). In PMS-AOPs, various reactive oxygen species (ROS), such as hydroxyl radical (•OH), sulfate radical (SO₄^{•-}), superoxide radical (O₂^{•-}) and singlet oxygen (¹O₂) are produced and participate in EOCs oxidation [1–5]. Among the various ROS, •OH (E₀ = 2.8 V) [6] and SO₄^{•-} (E₀ = 2.5–3.1 V) [7,8] possess higher redox potentials than O₂^{•-} (E₀ = 0.9 V) [9] and ¹O₂ (E₀ = 1.5 V) [9], which are more efficient for the degradation and mineralization of EOCs in aqueous solutions. However, on-demand production of specific radical species via PMS activation is still challenging, owing to the multiple chain reactions and pathways in PMS systems. Moreover, the ultrashort radical half-life span (1 μs for •OH and 30–40 μs for SO₄^{•-}) in the aqueous solution and thus short diffusion distance hampers their transport from the catalyst surface to the target organic pollutants for oxidation, resulting in unnecessarily high consumption of the oxidant [10,11]. In this regard, it is highly desirable to stabilize the radical species to secure

high selectivity and minimize chemical input in PMS-based AOPs.

In recent years, transition metals (TMs) immobilized in/on nanomaterials have demonstrated ultrahigh efficiency for PMS activation. For example, TMs-based metal-organic frameworks [12] as well as TMs supported on nanocarbons [13], carbon nitride (g-C₃N₄) [7] and metal oxides [14] were applied as heterogeneous PMS catalysts. However, some catalytic systems cannot selectively generate on-demand ROS, while others cannot stabilize the produced radical species, resulting in a dilemma in mineralization or chemical utilization efficiency. Moreover, the supported TM catalysts are usually vulnerable to harsh reaction conditions and suffer from metal leaching. Atomically dispersed metal sites, namely single-atom catalysts (SACs), have shown great application potential in PMS-based AOPs [15,16], owing to their high catalytic activity, desirable selectivity, and excellent durability [17–20]. Layered double hydroxides (LDHs) are known as cationic hydrotalcite-like clays. The positively charged hydroxide layers possess a significant number of intercalated and exchangeable anions, making LDHs good ion exchangers and adsorbents [21–24]. Moreover, the interlayers of LDH provide a confined microenvironment to immobilize the metal catalytic

* Corresponding author at: College of Geography and Environmental Science, Zhejiang Normal University, Jinhua 321004, China.

** Corresponding author.

E-mail addresses: dbwxl@zjnu.cn (X.-L. Wu), xiaoguang.duan@adelaide.edu.au (X. Duan).

¹ Chaofa Chen and Minjia Yan contributed equally to this work

sites, resembling nanochannels to initiate confined catalytic reactions. On account of the benefits of SACs and LDHs, immobilizing TM-SACs between the interlayers of LDHs may provide a platform for PMS activation under nanoconfinement.

In this study, single-atom Co (SA-Co) catalysts confined in LDHs were fabricated and applied as heterogeneous catalysts for PMS activation. The space-confined SA-Co catalyst exhibited high reactivity and stability for EOCs oxidation via Fenton-like reactions. The efficient and selective generation of the surface-bonded radical species in the SA-Co-LDH/PMS system was verified by competing anions, quenching experiments and electron paramagnetic resonance (EPR) spectroscopy. Besides, density functional theory (DFT) calculations also demonstrate the strong adsorption affinity of positively charged LDH with PMS, $\bullet\text{OH}$, SO_4^{2-} . Finally, the feasibility of SA-Co-LDH/PMS/PMS system for actual wastewater treatment was studied by building a catalytic membrane filtration system. This study provides a new tactic for in-situ generation of surface-stabilized radical species using nanoconfined SACs, and sheds new light on the development of cost-effective remediation systems.

2. Materials and methods

2.1. Synthesis of SA-Co-LDH

Details of the chemicals are provided in [Supporting Information](#), Text S1. The Cl^- -intercalated Mg/Al LDH (LDH-Cl) were prepared according to the literature (details in [Supporting Information](#), Text S1 and S2). To synthesize SA-Co-LDH, 5, 10, 15, 20-tetrakis(4-carboxyphenyl) porphyrin Co(II) (TCPP-Co) was intercalated into Mg/Al LDH via ion exchange with LDH-Cl ([Supporting Information, Scheme S1](#)). In general, 0.1 g of LDH-Cl was dispersed in 30 mL of deionized water under ultrasound for 15 min. Then, 0.01 g of TCPP-Co was dissolved in 5 mL of aqueous solution (pH 10) and added to the LDH-Cl suspension. The mixture solution was shaken in a water bath (30 °C) for 24 h to achieve the ion exchange of TCPP-Co with LDH-Cl. Then, the product was separated by filtration and dried in vacuum at 60 °C overnight. The SA-Co supported on layered double oxide (LDO) was obtained by the calcination of TCPP-Co intercalated Mg/Al LDH at 550 °C in the N_2 atmosphere for 2 h. SA-Co-LDO will experience reconstruction in the aqueous solution to form SA-Co-LDH.

2.2. Characterizations and computational details

The catalyst was characterized by using a scanning electron microscope (SEM, Hitachi S-4800), transmission electron microscope (TEM, JEM-2100F, Japan), aberration-corrected high-angle annular dark-field scanning TEM (HAADF-STEM, JEM-ARM200F, Japan), X-ray diffractometer (XRD, Shimadzu XRD-6000), X-ray photoelectron spectroscopy (XPS, Thermo Scientific ESCALAB 250) and N_2 adsorption-desorption measurements (Autosorb-I-MP system). The Co concentrations in the solution were analyzed by inductively coupled plasma mass spectrometry (ICP-MS, Thermo Scientific PlasmaQuad III, USA). Electron spin resonance (ESR) analysis was performed on a Bruker EPR I200 spectrometer. Raman spectra were collected using a Horiba Jobin Yvon LabRam instrument. Fourier transform infrared spectroscopy (FT-IR) spectroscopy spectra were collected by Attenuated total reflection Fourier transform infrared spectroscopy (ATR-FTIR, NEXUS 670, USA). The Co K-edge X-ray absorption fine structure (XAFS) spectroscopy was carried out using the RapidXAFS 1 M (Anhui Absorption Spectroscopy Analysis Instrument Co., Ltd.). Total organic carbon (TOC) analysis was performed using a TOC analyzer (Liqui TOC II, Elementar, Germany). The computational details are shown in [Supporting Information](#), Text S3.

2.3. Experimental procedures

Catalytic degradation of meropenem (MEM), a typical antibiotic,

was carried out in a magnetically stirred bottle (50 mL) using SA-Co-LDH as the catalyst and PMS as the oxidant. Generally, 30.0 mL reaction solution containing 0.1 g/L of suspending catalyst and 20 mg/L of MEM was stirred in the dark for 30 min to achieve the adsorption-desorption equilibrium. The catalytic degradation processes were initiated by adding PMS into the above suspension. At predetermined time intervals, 1.0 mL reaction suspension was sampled and quenched with 0.2 mL methanol. The mixture was filtered with a 0.22 μm membrane to separate the catalyst. The residual concentration of MEM in the separated solution was detected by high-performance liquid chromatography (HPLC). The used catalyst was separated, washed with deionized water several times for the recycling experiment, and dried at 65 °C. For quenching experiments, a desired amount of the quenching agent was added to the reaction solution prior to adding PMS. The concentration of PMS was spectrophotometrically detected by 2,2'-azino-bis (3-ethylbenzothiazoline-6-sulfonic acid) diammonium salt (ABTS) method [25].

3. Results and discussion

3.1. Characterization of the atomically dispersed Co sites

From the scanning electron microscope (SEM) images ([Fig. 1a](#) and S1) and transmission electron microscope (TEM) images ([Fig. 1b](#)), SA-Co-LDH exhibits a hexagonal plate-like morphology. As can be seen from the high-angle annular dark-field scanning transmission electron microscopy (HAADF-STEM) images ([Fig. 1c](#) and d) [26], the bright dots of atomic-size Co are evenly dispersed on LDH. The energy dispersive X-ray (EDX) mappings ([Fig. 1e-j](#)) show homogeneous distributions of N, O, Mg, Al and Co elements over the hexagonal nanoplates, indicating the successful implantation of Co element into the LDH substrate. The high-resolution TEM image ([Fig. S2](#)) shows the amorphous nature of SA-Co-LDH without lattice fringe for Co nanoparticles, suggesting the Co species are atomically dispersed on the LDH substrate. From the XRD patterns of SA-Co-LDH ([Fig. 1k](#)), the peaks at 11.7°, 23.6°, 35.0°, 39.5° and 47.1° are assigned to the (003), (006), (009), (015) and (018) planes of the Mg/Al LDHs, respectively. The absence of Co peaks in the XRD patterns also suggests that the Co element is atomically implanted in the LDH. Interestingly, the (003) peak of SA-Co-LDH shifted to a lower angle with increased TCPP-Co loading ([Fig. 1l](#)), owing to the increased interlayer spacing of LDH. This is also verified by the XPS analyses ([Fig. S3](#)), where Co element appeared with Cl element disappeared in the SA-Co-LDH after ion-exchanging of TCPP-Co with LDH-Cl. The TCPP-Co intercalated LDH with enlarged interlayer spacing is beneficial to free ions/molecule transportation and exposing more inner active surface [27], facilitating the mass transfer and catalytic reactions within the nanoconfined environment.

The elemental composition of SA-Co-LDH was determined by inductively coupled plasma mass spectrometry (ICP-MS) and XPS ([Table S1](#)). It was found that the SA-Co-LDH is composed of O, Mg, Al, C, N and Co elements. The Co content in SA-Co-LDH is determined to be ~0.5 % wt by ICP-MS. From the high-resolution Co 2p XPS spectra ([Fig. 1m](#)), the peaks for Co^{2+} and Co^{3+} can be observed with the absence of zero-valent Co [28,29]. Meanwhile, the N 1s XPS spectra of SA-Co-LDH ([Fig. S4](#)) are deconvoluted into three peaks at 398.5, 399.1 and 400.1 eV, owing to the pyridine N, pyrrolic N coordinated with Co ($\text{Co}-\text{N}_x$), and uncoordinated pyrrolic N, respectively [30,31]. These results suggest that the Co atoms are coordinated with the pyrrolic N. X-ray absorption near-edge structure (XANES) spectra ([Fig. 1n](#)) shows that the absorption edge of SA-Co-LDH was located between phthalocyanine cobalt (CoPc) and Co_3O_4 , confirming the Co atoms carry positive charges with average valence states between +2 and +3. As shown in [Fig. S5](#), EXAFS oscillations in k-space for CoPc and SA-Co-LDH have similar scattering paths, owing to their similar Co-N coordination structure [17]. The FT-EXAFS spectrum of SA-Co-LDH in R space ([Fig. 1o](#)) displays one prominent peak at 1.5 Å, corresponding to the Co–N first coordination shell, and no Co–Co coordination peak at 2.2 Å

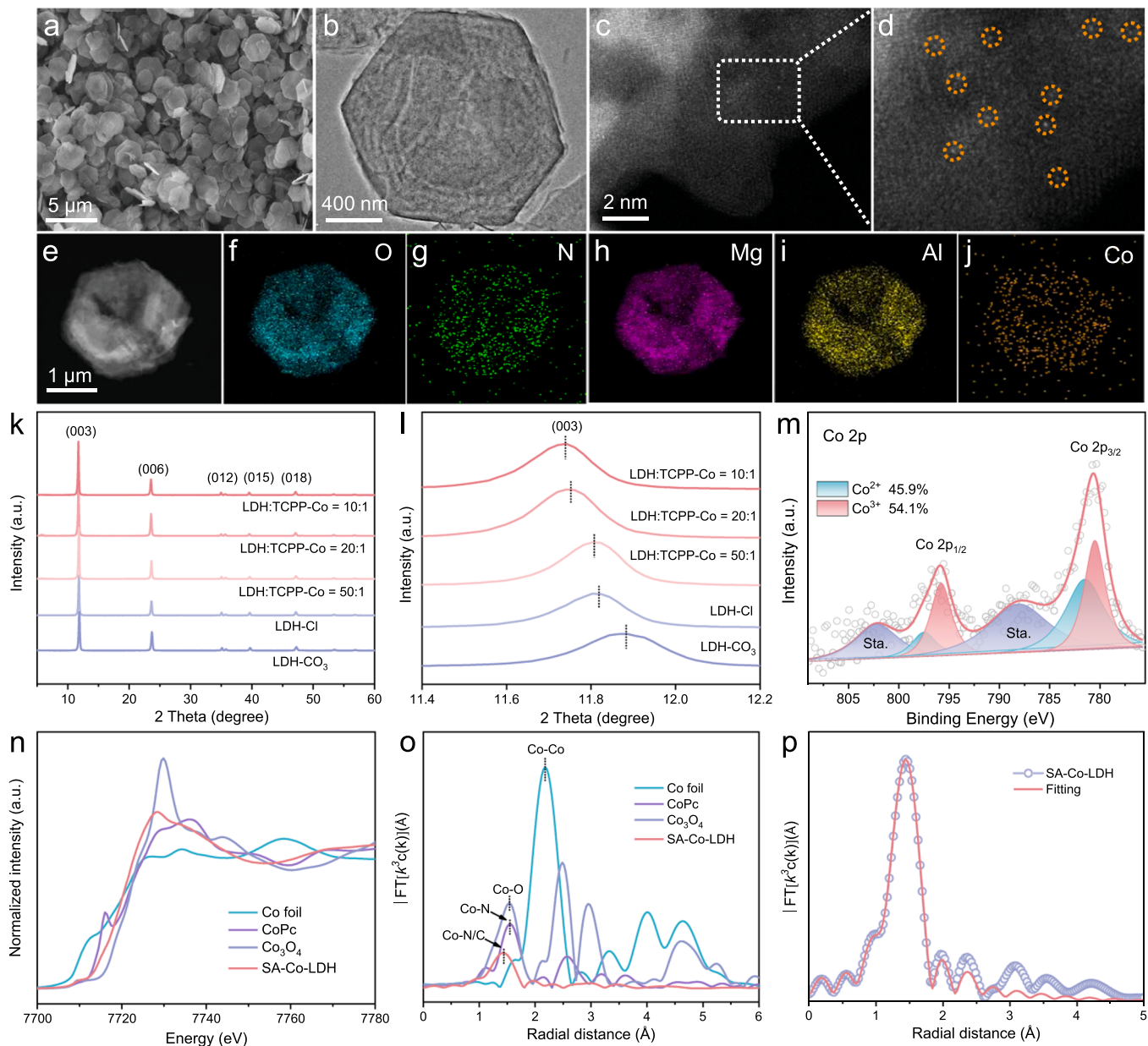


Fig. 1. (a) SEM image. (b) TEM image. (c) HAADF-STEM image and (d) the enlarged view of SA-Co-LDH. (e-j) The corresponding EDX mapping of SA-Co-LDH. (k) XRD pattern and (l) the enlarged view of the XRD pattern of SA-Co-LDH. (m) High resolution Co 2p XPS. (n) Normalized Co K-edge XANES spectra of Co foil, CoPc, Co_3O_4 , and SA-Co-LDH. (o) The k^3 -weighted Fourier transform EXAFS spectra at R space and (p) the corresponding EXAFS fitting curves.

can be detected. The EXAFS fitting of the first shell in R space (Fig. 1p) and the corresponding fitting parameters (Table S2) revealed that the coordination number of Co atoms is 3.9 with a bond distance of 1.89 Å. As observed in the wavelet transform (WT) plots (Figs. S6a-6d), the WT maximums of CoPc and SA-Co-LDH are located at $\sim 5 \text{ \AA}^{-1}$, corresponding to the Co–N bonding [32–34], while the WT maximum for Co–Co bonds cannot be observed for SA-Co-LDH. These results demonstrate the successful fabrication of the Co–N₄ single-atom sites confined in the interlayer of LDH. The Co single sites within the nanolayers and the positively charged LDH substrate are beneficial to heterogeneous catalysis by preconcentrating the anionic reactants and accelerating the redox reactions under nanoconfinement.

3.2. Catalytic performance of the SA-Co-LDH

We selected meropenem (MEM) as a model EOCs to evaluate the catalytic performance of SA-Co-LDH for Fenton-like reactions. The

dosages of PMS and catalyst were optimized as 0.2 and 0.1 g/L, respectively (Fig. S7 and S8). As illustrated in Fig. S9, the SA-Co-LDH/PMS system exhibited a wide operating pH window (pH 3–11) with the MEM degradation efficiencies were all greater than 97 %. In addition, Co ion leaching from SA-Co-LDH is below 50 µg/L over all the test pH range (Table S3), which is lower than the recommended limits in reclaimed water (50 µg/L) by US EPA [14]. The wide pH adaptability and structural robustness of SA-Co-LDH could be attributable to the strong affinity between LDH and immobilized single Co sites under nanoconfinement. From Fig. 2a, MEM can be rapidly eliminated in the SA-Co-LDH/PMS system within 10 min, while MEM was barely removed by PMS, LDH or SA-Co-LDH alone. The pure Mg/Al LDH and the homogeneous TCPP-Co counterpart were inefficient in activating PMS and oxidizing MEM. Therefore, the nanoconfined SA-Co sites have significantly boosted the catalytic performance of SA-Co-LDH. Furthermore, the degradation kinetics of MEM were fitted by the first-order kinetic model ($-\ln(C/C_0) = k_{\text{obs}}$) [35] and the corresponding observed kinetic

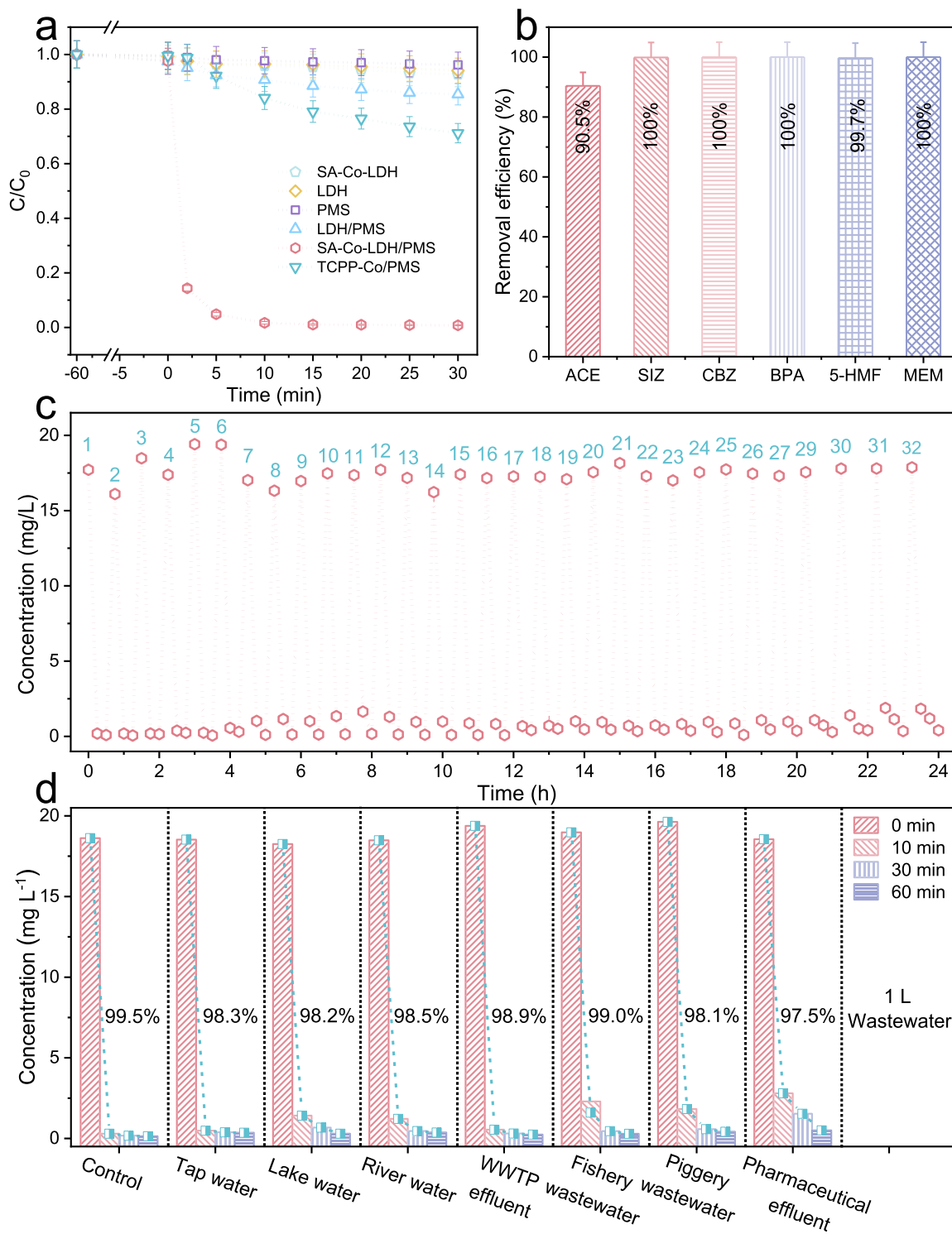


Fig. 2. (a) MEM degradation in the SA-Co-LDH, LDH, PMS, LDH/PMS, SA-Co-LDH/PMS, TCPP-Co/PMS systems. (b) Degradation of various EOCs in the SA-Co-LDH/PMS system. (c) A 24 h continuous cyclic test for MEM degradation in the SA-Co-LDH/PMS system. (d) MEM degradation in the various water matrices. (Reaction conditions: [LDH] = [SA-Co-LDH] = 0.10 g/L, [TCPP-Co]₀ = 30 μ M, [SIZ]₀ = [CBZ]₀ = [BPA]₀ = [MEM]₀ = 20 mg/L, [ACE]₀ = [5-HMF]₀ = 10 mg/L, [PMS]₀ = 0.20 g/L, pH 7.0).

rate constant (k_{obs}) is shown in Fig. S10. The obtained k_{obs} of SA-Co-LDH/PMS (0.375 min^{-1}) system is 20 and 52 times greater than that of TCPP-Co/PMS (0.018 min^{-1}) and LDH/PMS (0.007 min^{-1}) systems, respectively, confirming the exceptionally high activity of SA-Co-LDH. The decomposition and utilization efficiency of PMS was evaluated by measuring the residual concentration of PMS during the reaction (Fig. S11). The stoichiometric efficiency of PMS (amount of

MEM degraded by per unit of PMS) was calculated to be 0.37 and PMS consumption on 30 min is about 70 % (Fig. S11). Besides, the concentration of the relevant sulfate by-product produced by decomposition of PMS was determined (Fig. S12). The concentration of sulfate ion (111 ppm) is below the USEPA secondary maximum contaminant level (250 ppm) for sulfate in drinking water [36]. Considering the differences in reaction conditions and types of organic pollutants, a

normalized kinetic model ($k\text{-value} = k_{obs} \cdot C_0 / [\text{PMS}]_0 \cdot [\text{Cat.}]_0$) was applied to evaluate the efficacy of the Fenton-like systems [37]. The $k\text{-value}$ of SA-Co-LDH is much larger than that of the state-of-the-art SACs for degradation of EOCs via PMS activation (Fig. S13, Table S4), confirming the high efficacy of the SA-Co-LDH mediated Fenton-like system. Moreover, the SA-Co-LDH/PMS system outperforms the benchmark homogeneous and heterogeneous cobalt systems of $\text{Co}^{2+}/\text{PMS}$ and $\text{Co}_3\text{O}_4/\text{PMS}$ and requires the lowest Co consumption (Fig. S14a-14b). The nanoconfined SA-Co sites remarkably increase the catalytic activity of LDH and improve atomic cobalt efficiency, thus dramatically reducing metal usage. Additionally, the nanoconfined system is highly effective in the purification of diverse EOCs (Fig. 2a and S15), including antibiotics (MEM, sulfisoxazole (SIZ)) [38], endogenous pollutants (bisphenol (BPA), 5-hydroxymethylfurfural (5-HMF)),

pesticides (acetamiprid (ACE)) and antiepileptic drugs (carbamazepine (CBZ)). Furthermore, the SA-Co-LDH/PMS system also showed excellent performances in cyclic batch experiments (32 cycles), where the MEM degradation efficiencies maintained over 97 % after the 24 h continuous operating (Fig. 2c). The SA-Co-LDH after recycling was characterized by SEM, XRD, XPS and EXAFS. It was found that the SA-Co-LDH still maintained its original morphology and crystal structure after the cyclic test (Fig. S16). Moreover, the XPS and XAFS spectra demonstrated that the composition and coordination structure of the SA-Co-LDH were unchanged after reaction (Fig. S17, Table S2). These results collectively suggest that SA-Co-LDH has excellent reusability and stability for the heterogeneous PMS activation. What's more, the performances of the SA-Co-LDH/PMS system for treatment of MEM in real water and wastewater matrices were tested. To highlight the potential of

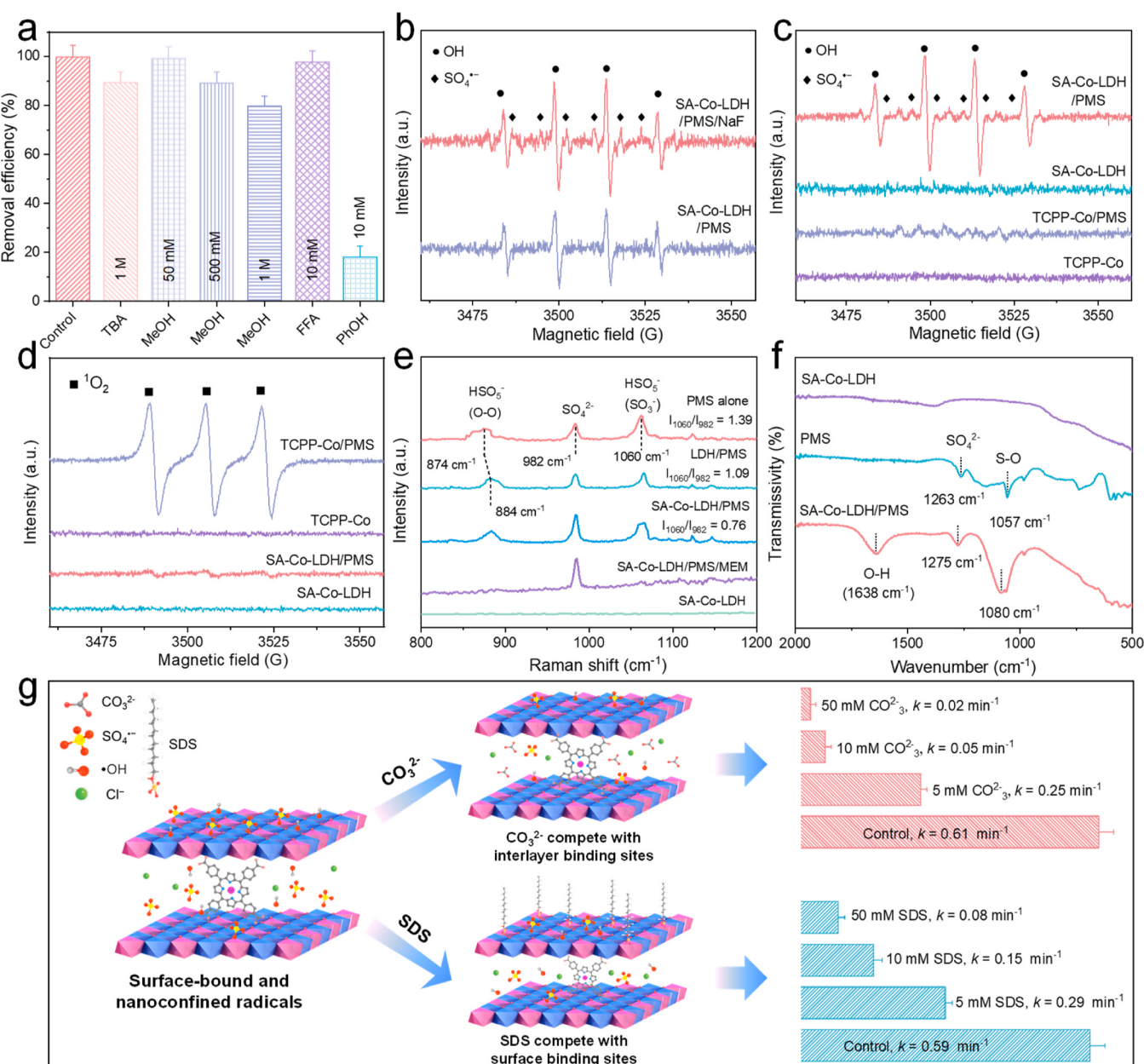


Fig. 3. (a) Quenching experiments for the degradation of MEM in the SA-Co-LDH/PMS system. (b) DMPO spin-trapping EPR spectra of 290 the SA-Co-LDH/PMS system with the presence and absence of NaF. (c) DMPO spin-trapping EPR spectra. (d) TEMP spin-trapping EPR spectra (• represents DMPO-•OH, ◆ represents DMPO- SO_4^{2-} and ■ represents TEMP- $^1\text{O}_2$). (e) *In situ* Raman spectra of SA-Co-LDH, PMS alone, SA-Co-LDH/PMS and SA-Co-LDH/PMS/MEM. (f) *In situ* ATR-FTIR spectra of SA-Co-LDH, PMS alone and SA-Co-LDH/PMS and (g) schematic illustration of the competing effects of SDS and CO_3^{2-} , kinetic plots for MEM degradation in the SA-Co-LDH/PMS system under the various competing conditions.

SA-Co/LDH/PMS for practical wastewater treatment, we scaled up our testing system from 30 mL to 1.0 L. In all these cases, SA-Co/LDH/PMS system showed impressive catalytic activity, achieving high MEM removal efficiencies (>98 %) in the various water matrices (tap water, lake water, river water, wastewater treatment plant (WWTP) effluent, fishery wastewater, piggery wastewater and pharmaceutical effluent) (Fig. 2d). These results imply that SA-Co-LDH-mediated Fenton-like reaction has an outstanding selectivity and application potential for practical wastewater treatment.

3.3. Generation and stabilization of the reactive species

Quenching experiments were further conducted to probe ROS in the SA-Co-LDH/PMS system. Tert-butyl alcohol (TBA, $k(\bullet\text{OH}) = 7.6 \times 10^8 \text{ M/s}$) and methanol (MeOH, $k(\bullet\text{OH}) = 9.7 \times 10^8 \text{ M/s}$ and $k(\text{SO}_4^{\bullet-}) = 3.2 \times 10^6 \text{ M/s}$) were used as the corresponding radical quenchers [25, 39]. Furfur alcohol (FFA, $k(^1\text{O}_2) = 1.20 \times 10^8 \text{ M/s}$) and phenol (PhOH, $(k(\text{SO}_4^{\bullet-}) = 8.8 \times 10^9 \text{ M}^{-1} \text{ s}^{-1}$, $k(\bullet\text{OH}) = 6.6 \times 10^9 \text{ M}^{-1} \text{ s}^{-1}$) were selected as the scavengers for $^1\text{O}_2$ and surface-bound radicals, respectively [39,40]. As shown in Fig. 3a and S18, the removal efficiency of MEM slightly decreased from ~99 to 89 %, 80 % and 88 % with the presence of TBA (1 M), MeOH (1 M) and FFA (10 mM), respectively, indicating MEM oxidation did not rely on dissolved free radicals and $^1\text{O}_2$ in the bulk solution. Furthermore, replacing of H_2O with D_2O to prolong the life span of $^1\text{O}_2$ shows almost no impact on MEM degradation in the SA-Co-LDH/PMS system (Fig. S19), verifying the insignificant role of $^1\text{O}_2$ in MEM oxidation. It is noteworthy that MEM removal was not well suppressed when excessive MeOH was added in the reaction system, which is indicative of the presence of surface-bound radical species [41, 42]. Adding PhOH into the SA-Co-LDH/PMS system resulted in significantly declined MEM removal (18 %), suggesting that the surface-bound radicals are the dominant ROSSs for the oxidation of MEM [41]. As radicals are in situ generated in the SA-Co-LDH/PMS system, they may be confined within the positively charged LDH layers to form the surface-bound radicals. To validate this assumption, the electron paramagnetic resonance (EPR) characterizations of the SA-Co-LDH/PMS system before and after adding F^- ions were carried out, because F^- ions can promote the release of surface-bound radicals into the bulk solution [42]. As shown in Fig. 3b, the intensities of DMPO-•OH and DMPO- $\text{SO}_4^{\bullet-}$ signals were remarkably enhanced after adding 10 mM of NaF into the SA-Co-LDH/PMS system. The phenomenon indicated that the surface-bound •OH and $\text{SO}_4^{\bullet-}$ radicals were released into the aqueous solution. Overall, these results collectively imply that the surface-bound radicals have played a dominant role in MEM oxidation.

EPR spectroscopy was applied to identify ROS in the reaction systems using 5,5-dimethyl-1-pyrroline-N-oxide (DMPO) and 2,2,6,6-tetramethyl-4-piperidone (TEMP) as the spin trapping reagents for radicals ($\bullet\text{OH}$ and $\text{SO}_4^{\bullet-}$) and $^1\text{O}_2$, respectively. No obvious signals for •OH, $\text{SO}_4^{\bullet-}$ and $^1\text{O}_2$ (Figs. S20a-20b) were observed in the LDH and LDH/PMS systems, indicating pure LDH is inert for catalysis. In addition, strong radical signals (DMPO-•OH and DMPO- $\text{SO}_4^{\bullet-}$) in the SA-Co-LDH/PMS system were observed, but no radical species were detected in the homogeneous TCPP-Co/PMS system (Fig. 3c). On the contrary, strong TEMP- $^1\text{O}_2$ signals can be detected in the TCPP-Co/PMS system but not in the SA-Co-LDH/PMS system (Fig. 3d). This interesting phenomenon indicates that nanoconfined Co catalytic sites in LDH facilitated the selective generation of highly oxidizing radical species and prohibited the production of less-reactive $^1\text{O}_2$, which is generally produced via the self-decomposition of PMS ($\text{HSO}_5^- + \text{SO}_5^{2-} \rightarrow \text{SO}_4^{2-} + \text{HSO}_4^- + ^1\text{O}_2$). Thus, the negatively charged PMS can be stabilized by the positively charged LDH and prohibited its self-decomposition and minimized ineffective PMS consumption. As can be seen from the TEM elemental mapping of PMS-adsorbed SA-Co-LDH (Fig. S21), the S element was evenly distributed over the SA-Co-LDH nanosheets, confirming efficient adsorption and stabilization of PMS and $\text{SO}_4^{\bullet-}$ by SA-Co-LDH. As a result, the nanoconfined SA-Co sites in LDH could in-situ activate the surface-stabilized

PMS to rapidly generate the surface-bound •OH and $\text{SO}_4^{\bullet-}$ radicals [43]. These radical species possess high redox potentials and can effectively degrade and mineralize the organic pollutants, achieving a high TOC removal (83 %) in the SA-Co-LDH/PMS system (Fig. S22). In summary, the SA-Co-LDH system exhibits high catalytic efficiency for PMS activation and high selectively for production of the surface-bound radicals to attain fast and deep oxidation of EOCs.

PMS adsorption and evolution on the surface of SA-Co-LDH was investigated by in-situ Raman and attenuated total reflectance Fourier transform infrared (ATR-FTIR) spectroscopy. As shown in Fig. 3e, the Raman peaks at 1060 and 982 cm^{-1} are assigned to HSO_5^- and SO_4^{2-} , respectively [44]. The intensity ratio of I_{1060}/I_{982} (0.76) in SA-Co-LDH/PMS is much smaller than free PMS (1.39), suggesting the efficient activation and transformation of PMS (HSO_5^-) into SO_4^{2-} . Notably, the Raman peak for the O-O stretching vibration of HSO_5^- shifts from 884 to 874 cm^{-1} in the SA-Co-LDH/PMS system, which is attributed to the strong surface interactions between the negatively charged HSO_5^- and the positively charged LDH layers. Furthermore, once MEM was added to the SA-Co-LDH/PMS system, all PMS-associated peaks vanished and only the peak of SO_4^{2-} remained, indicating the PMS was decomposed into SO_4^{2-} during the catalytic oxidation process. ATR-FTIR spectrum of PMS (Fig. 3f) shows significant characteristic peaks of S–O (1057 cm^{-1}) and $\text{SO}_4^{2-}/\text{SO}_4^{2-}$ (1263 cm^{-1}) [40,45], while these peaks were blue-shifted in the SA-Co-LDH/PMS system, indicating the strong interaction between the PMS/ $\text{SO}_4^{2-}/\text{SO}_4^{2-}$ and the SA-Co-LDH. In addition, a new peak at $\sim 1638 \text{ cm}^{-1}$ was observed in SA-Co-LDH/PMS, ascribed to the O–H bending vibration for surface-adsorbed hydroxyl groups [46], implying the generation of surface-bound •OH. We further employed organic and inorganic anions to compete with the surface-bonded radicals (Fig. 3g). Sodium dodecyl sulfate (SDS) with a long carbon chain and CO_3^{2-} with strong binding affinity to LDH interlayers were applied as the competing anions. MEM removal is prohibited when adding SDS or CO_3^{2-} into the SA-Co-LDH/PMS system (Fig. S23). The MEM degradation kinetics gradually decreased with increased SDS and CO_3^{2-} concentrations, owing to the suppressed generation of the surface-bonded radicals. To sum up, we believe that surface-bound radicals are the main reactive substances in SA-Co-LDH/PMS system.

We supposed that the negatively charged catalyst surface will effectively adsorb and stabilize of the negatively charged PMS to realize high selectivity and reactivity for radicals production. Adsorption experiments of PMS onto LDH and SA-Co-LDH were carried out. Compared to low PMS adsorption onto pure LDH (Fig. 4a), PMS adsorption onto SA-Co-LDH (Fig. 4b) was increased linearly with the increase of initial PMS concentrations. Plots of PMS adsorption vs. initial PMS concentrations are shown in Fig. S24, and the slope for PMS onto SA-Co-LDH was 3 times of that onto pure LDH. The adsorption capacity of PMS onto SA-Co-LDH is about 1.8 and 4.6 times of that onto pure LDH and Co_3O_4 , respectively (Fig. 4c). The enhanced PMS adsorption onto the SA-Co-LDH is beneficial to its nanoconfined catalysis to produce the surface-bound radicals. Zeta-potential analysis (Fig. 4d) suggested that the SA-Co-LDH (4.5 mV) carries more positive charge than the pure LDH (3.2 mV) and the Co_3O_4 (-26.0 mV), which provides more binding sites for the negatively charged PMS. Thus, this nanoconfined catalytic system may facilitates the in-situ activation of PMS to selective production of surface-bound radicals, owing to the surface-stabilization effect. In addition, the interaction of PMS (HSO_5^-), •OH and $\text{SO}_4^{\bullet-}$ with LDH was simulated by DFT calculations. The adsorption sites at the surface and within the interlayer of LDH were considered and the corresponding adsorption configurations were optimized in Fig. 4e and f. The adsorption energies (E_{ad}) of HSO_5^- , •OH and $\text{SO}_4^{\bullet-}$ were all smaller than -170 eV , suggesting their strong adsorption affinity toward LDH. Owing to the extremely strong adsorption capacity of SA-Co-LDH toward surface-bound radicals, we speculate that this ingenious nanoconfined structure may prolong the production of the surface-bound radical species and inhibit their decay. To verify this conjecture, we monitored

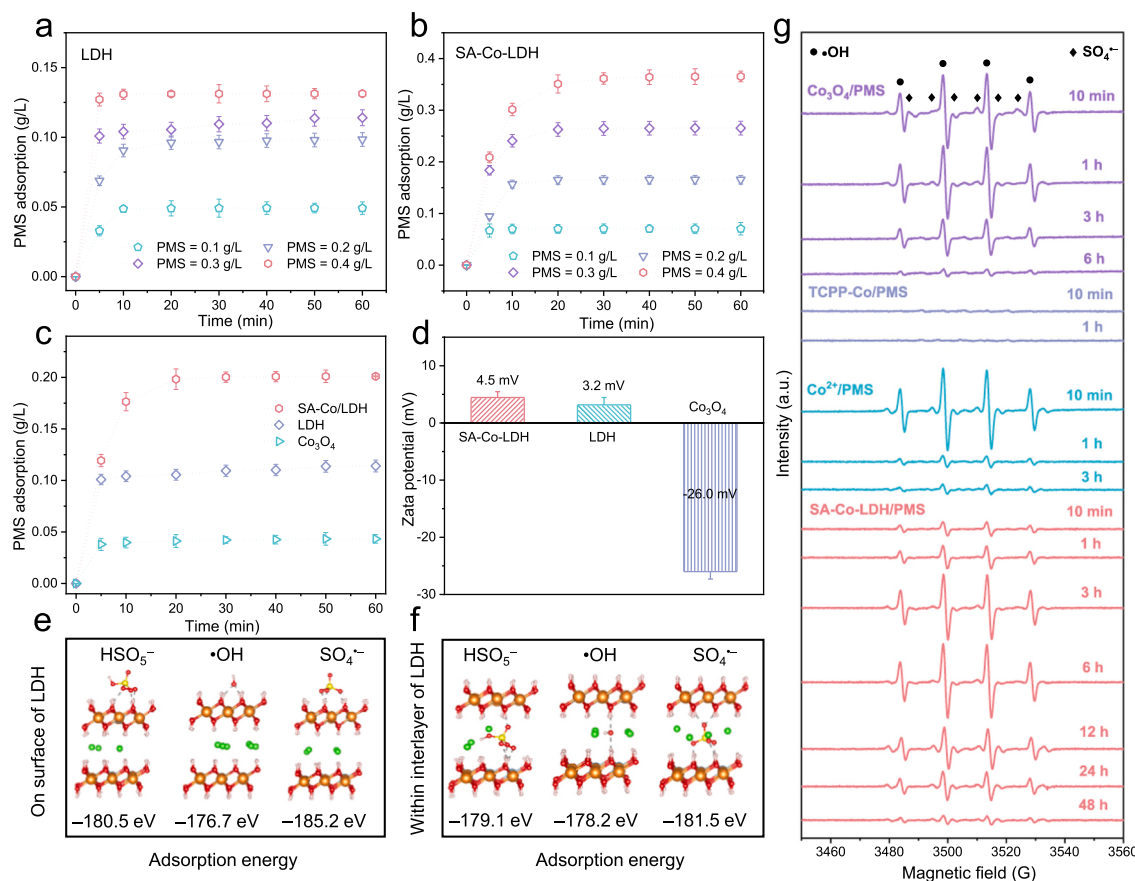


Fig. 4. PMS adsorption onto (a) LDH and (b) SA-Co-LDH under various PMS dosages. (c) PMS adsorption onto LDH, SA-Co-LDH and Co_3O_4 ($[\text{PMS}]_0 = 0.2 \text{ g/L}$, $[\text{catalyst}] = 0.1 \text{ g/L}$, $\text{pH} = 6.8$, and $T = 25^\circ\text{C}$). (d) Zeta potential of the LDH, SA-Co-LDH and Co_3O_4 . (e) The adsorption of HSO_5^- , $\bullet\text{OH}$ and $\text{SO}_4^{\bullet-}$ (e) on the surface and (f) within the interlayer of LDH. (g) Time-dependent DMPO-spin trapping EPR spectroscopy in the SA-Co-LDH/PMS, $\text{Co}^{2+}/\text{PMS}$, TCPP-Co/PMS and $\text{Co}_3\text{O}_4/\text{PMS}$ systems. (Reaction conditions: $[\text{SA-Co-LDH}]_0 = [\text{Co}_3\text{O}_4]_0 = [\text{TCPP-Co}]_0 = 0.10 \text{ g/L}$, $[\text{Co}^{2+}]_0 = 20 \mu\text{M}$, $[\text{PMS}]_0 = 0.20 \text{ g/L}$, $\text{pH} = 7.0$.

the EPR signals of the radical species in the Co-LDH/PMS system and the benchmark homogeneous and heterogeneous cobalt systems over time. Fig. 4g shows the appearance of strong DMPO- $\bullet\text{OH}$ and DMPO- $\text{SO}_4^{\bullet-}$ signals within 10 min in typical homogeneous $\text{Co}^{2+}/\text{PMS}$ and heterogeneous $\text{Co}_3\text{O}_4/\text{PMS}$ systems. As expected, the signals were gradually decayed within 3 h in the $\text{Co}^{2+}/\text{PMS}$ system and 6 h in the $\text{Co}_3\text{O}_4/\text{PMS}$ system due to radicals' self-quenching or further reaction with the solvent. Distinctly, signals for DMPO- $\bullet\text{OH}$ and DMPO- $\text{SO}_4^{\bullet-}$ increase progressively in the SA-Co-LDH/PMS system within 3 h and can last up to 48 h, implying the continuous generation and preservation of the surface-bound radical species. Thus, the in-situ produced $\bullet\text{OH}$ and $\text{SO}_4^{\bullet-}$ radicals via PMS activation by the nanoconfined SA-Co sites were stabilized by LDH, leading to prolonged lifespans and inhibited self-quenching.

To corroborate the above findings, we applied laser flash photolysis and fluorescence spectroscopy to probe the lifetime of $\text{SO}_4^{\bullet-}$ radical and its reaction behavior with pollutants, respectively. Details for the experiments of laser flash photolysis and fluorescence spectroscopy can be found in the Supporting Information (Text S11). For laser flash photolysis, $\text{SO}_4^{\bullet-}$ radical was produced by photolysis of persulfate (PS) using a 266 nm laser pulse, and the adsorption signals of $\text{SO}_4^{\bullet-}$ radical was monitored at 450 nm [47]. The transient absorption spectra of $\text{SO}_4^{\bullet-}$ radical with and without the presence of LDH were monitored. From the results of laser flash photolysis (Fig. S25), the calculated average lifetime (τ_A) of the free $\text{SO}_4^{\bullet-}$ radical is 43.26 μs , and half-life time ($\ln 2 \tau_A$) of $\text{SO}_4^{\bullet-}$ is 30.0 μs , which is consistent with the previous reported value (30–40 μs) [48]. As expected, with the presence of LDH, the τ_A and half-life time of $\text{SO}_4^{\bullet-}$ were prolonged to 82.58 and 57.2 μs , respectively,

confirming the longer life-span of the surface-bound $\text{SO}_4^{\bullet-}$. The life-span of the surface-bound $\text{SO}_4^{\bullet-}$ radical was almost doubled (~1.9 times) as compared to that of free $\text{SO}_4^{\bullet-}$ radical, which facilitates its interaction with the target pollutant and increases its utilization efficiency [48]. Naproxen (NAP), a common analgesic and antipyretic drugs, can be efficient chemiluminescent probe for real-time quantification of $\text{SO}_4^{\bullet-}$ radical (Fig. S26a) [49]. From the steady-state fluorescence (FL) spectra (Fig. S26b and S26c), it was found that the FL intensity of the heterogeneous SA-Co-LDH/PMS/NAP system was higher than that of the homogeneous $\text{Co}^{2+}/\text{PMS}/\text{NAP}$ system, suggesting more NAP was oxidized by the surface bound $\text{SO}_4^{\bullet-}$ radical than by the free $\text{SO}_4^{\bullet-}$ radical. This result indicates that more $\text{SO}_4^{\bullet-}$ radical was produced and less self-quenching of the surface bound $\text{SO}_4^{\bullet-}$ radical in the heterogeneous system. In addition, the FL decay lifetime in the SA-Co-LDH/PMS/NAP system (12.52 ns) was longer than that of the homogeneous $\text{Co}^{2+}/\text{PMS}/\text{NAP}$ system (6.41 ns) (Fig. S26d), confirming more efficient oxidation of NAP by surface-bound $\text{SO}_4^{\bullet-}$ radical to produce the fluorescence intermediates. These results collectively demonstrated that the surface-bound $\text{SO}_4^{\bullet-}$ radical has longer life-span and was more efficient for oxidation of pollutants. This phenomenon greatly benefits practical soil remediation and wastewater treatment by providing long-lasting ROS, minimizing PMS consumption, enhancing oxidation efficiency and reducing operating costs.

The SA-Co-LDH also exhibited high adsorption capacity toward MEM (396.8 mg/g) (Fig. S27, Table S5), which facilitates the preconcentration and in-situ degradation of target pollutants by surface-bound radicals. As a result, the negatively charged PMS can be preconcentrated and stabilized on the surface of SA-Co/LDH, which will be activated by

surrounding Co single sites for continuous and selective generation of the radical species. Furthermore, the in-situ produced $\bullet\text{OH}$ and $\text{SO}_4^{\bullet-}$ radicals will adsorb on inactive LDH to form the surface-bound radicals, thereby inhibiting their self-quenching. Finally, the organic pollutants in the aqueous solution diffused to and accumulated in the LDH layers, which were immediately attacked by the surface-bound radicals, leading to efficient degradation and mineralization of EOCs under nano-confinement. The intermediate products and degradation pathways for MEM oxidation in the SA-Co/LDH/PMS system are shown in Fig. S28 and S29, respectively. Detailed discussions can be found in the Supporting Information (Text S12).

3.3.1. The design of a membrane filtration reactor

To study the practical application of the SA-Co/LDH/PMS system for wastewater treatment, a SA-Co/LDH-based membrane filtration device was constructed (Fig. 5a-c). The membrane technology is more sustainable and convenient than the dispersed catalyst suspensions. In this experiment, SA-Co/LDH membranes were prepared by vacuum-assisted

filtration of SA-Co/LDH suspensions onto the polyethersulfone (PES, pore size $\sim 0.22 \mu\text{m}$ and diameter $\sim 5 \text{ cm}$) substrate membrane (Fig. 5d, e). The SA-Co/LDH/PES membrane has excellent flexibility and adhesion, so that the catalyst will not separate from the membrane during the catalytic reaction. Compared with the water contact angle (WCA) of the pristine PES membrane ($\sim 53.5^\circ$), the WCA of the SA-Co/LDH/PES membrane ($\sim 32.5^\circ$) is significantly reduced (Fig. 5f, g), indicating that the SA-Co/LDH/PES membrane is extremely hydrophilic, which will reduce water transport resistance and suppresses the membrane fouling. The cross-sectional and plane SEM images of SA-Co/LDH/PES membrane showed that the SA-Co/LDH catalyst layer was evenly deposited on the PES membrane surface with thickness of $\sim 128 \mu\text{m}$ (Fig. 5h-j). The two-dimensional layered structure and interlayer porosity of the SA-Co/LDH endow the SA-Co/LDH/PES membrane with high flux and provide abundant adsorption and catalytic sites for PMS activation and contaminants' oxidation. We studied the SA-Co/LDH/PES/PMS system for the treatment of MEM spiked secondary effluent from local wastewater treatment plants (WWTPs) (Jinhua, China). As

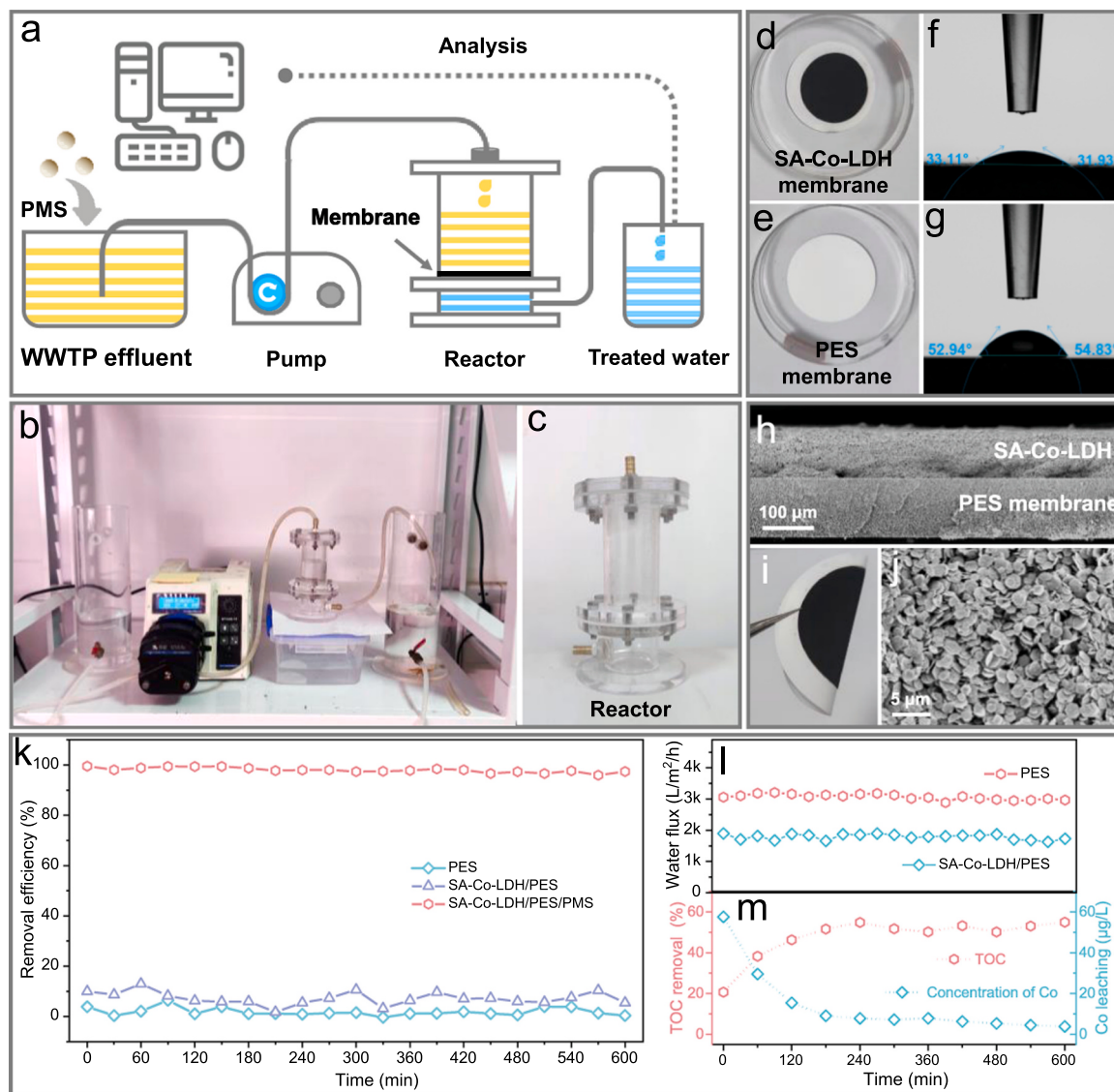


Fig. 5. Design of the catalytic membrane filtration device and its application for wastewater treatment. (a)Schematic illustration of the set-up for membrane filtration system. (b, c)Photograph of the membrane filtration system. (d, e)Photograph of the SA-Co/LDH/PES catalytic membrane and the pure PES membrane and (f, g) contact angles of the SA-Co/LDH/PES membrane and the PES membrane with water. SEM images of (h) cross-sectional and (i, j) surface of the SA-Co/LDH/PES membrane. (k)MEM removal in the SA-Co/LDH/PES/PMS, SA-Co/LDH/PES and the PES filtration systems. (l)Water flux of SA-Co/LDH/PES membrane and pristine PES membrane in wastewater treatment. (m) TOC removal and Co leaching concentration in the effluent by using the SA-Co/LDH/PES/PMS systems. (Working conditions: $[\text{MEM}]_0 = 20 \text{ mg/L}$, $[\text{PMS}]_0 = 0.2 \text{ g/L}$, pH.

shown in Fig. 5k, the SA-Co/LDH/PES membrane system maintained a high MEM removal efficiency (>98 %) over the 600 min of continuous operation, which demonstrates that the SA-Co/LDH/PES membrane system has a high stability and performance for wastewater treatment. In addition, the pure water flux of the SA-Co/LDH/PES membrane was maintained over ~1750 L/m²/h during the continuous operation (Fig. 5l), demonstrating its high-water permeability. More importantly, the system also exhibited extremely high resistance to catalyst leaching and pollutant mineralization (Fig. 5m). As shown in Fig. 5m, the Co leaching is gradually decreased and eventually stabilized (< 5 µg/L). This could be due to the fact that the physically adsorbed TCPP-Co on the surface of SA-Co-LDH can be easily desorbed, while the nanoconfined TCPP-Co within the interlayer of LDH was much more stable, resulting in much lower Co-leaching with increasing of reaction time. Thus, one can conclude that the SA-Co/LDH/PES membrane system is promising for EOCs removal from wastewater.

4. Conclusion

The radical species are demonstrated to be the most potent ROSs in AOPs. PMS-AOPs are efficient in producing •OH and SO₄²⁻ radicals, which have shown great promise for water treatment and soil remediation. However, the short lifespan and self-quenching of the radical species lead to the large consumption of the metal catalyst and oxidant in the conventional PMS-AOPs. As far as we know, the green and sustainable generation of long-life radical species with lower consumption of the metal catalyst and oxidant is still a challenge. In this study, we delicately embedded SA-Co sites into inactive LDH layers. The SA-Co-LDH provided a nanoconfined platform for the selective generation of surface-bound radicals via in-situ activation of PMS. The positively charged LDH can stabilize PMS and confine the generated radicals on the surface, which minimizes PMS self-decomposition and radical self-quenching to improve PMS utilization efficiency. As revealed by experimental and theoretical calculations, this surface-stabilization strategy allowed the continuous generation of the surface-bound •OH and SO₄²⁻ for efficient degradation and mineralization of MEM within the LDH layers. The SA-Co-LDH/PMS system also exhibited a wide operating pH range, excellent reusability and high efficiency for eliminating diverse EOCs, endowing SA-Co-LDH a great potential for practical wastewater treatment. This study showed the synergy of SACs and positively charged LDH substrates for in-situ generation and stabilization of radical ROS, providing a new tactic for maximizing the performance of heterogeneous Fenton-like systems with low chemical input and high mineralization efficiency.

CRediT authorship contribution statement

Chaofa Chen: Data curation, Formal analysis, Writing & editing. **Minjia Yan:** Methodology, Data curation, Formal analysis. **Yu Li:** Methodology, Data curation, Formal analysis. **Yuwen Hu:** Methodology, Data curation, Formal analysis. **Jianrong Chen:** Methodology, Investigation, Funding acquisition. **Xiaoguang Duan:** Writing - review & editing, Supervision. **Shaobin Wang:** Editing, Supervision. **Xi-Lin Wu:** Writing - review & editing, Supervision.

Declaration of Competing Interest

The authors declare that they have no known competing financial interests or personal relationships that could have appeared to influence the work reported in this paper.

Data Availability

Data will be made available on request.

Acknowledgements

X.-L. W. acknowledges the financial support from the Independent Designing Scientific Research Project of Zhejiang Normal University (2020ZS0302), J. C. acknowledges the Key R&D Project of Zhejiang Province (No. 2021C03163). X.D. acknowledges the financial support from Australian Research Council (DE210100253). The authors acknowledge Shenzhen HUASUAN Technology Co. LTD for helping with the DFT calculations and Dr. Yang Yang from Dalian institute of chemical physics (Chinese Academy of Sciences) for assistance of the laser flash photolysis experiments.

Appendix A. Supporting information

Supplementary data associated with this article can be found in the online version at doi:10.1016/j.apcatb.2023.123218.

References

- [1] X. Mi, P. Wang, S. Xu, L. Su, H. Zhong, H. Wang, Y. Li, S. Zhan, Almost 100% peroxymonosulfate conversion to singlet oxygen on single-atom CoN₂₊₂ sites, *Angew. Chem. Int. Ed.* 60 (2021) 4588–4593, <https://doi.org/10.1002/anie.202014472>.
- [2] Y. Chen, G. Zhang, H. Liu, J. Qu, Confining free radicals in close vicinity to contaminants enables ultrafast fenton-like processes in the interspacing of MoS₂ membranes, *Angew. Chem. Int. Ed.* 58 (2019) 8134–8138, <https://doi.org/10.1002/anie.201903531>.
- [3] L. Zhu, J. Ji, J. Liu, S. Mine, M. Matsuoka, J. Zhang, M. Xing, Designing 3D-MoS₂ sponge as excellent cocatalysts in advanced oxidation processes for pollutant control, *Angew. Chem. Int. Ed.* 59 (2020) 13968–13976, <https://doi.org/10.1002/anie.202006059>.
- [4] Y. Zhao, H. An, J. Feng, Y. Ren, J. Ma, Impact of crystal types of AgFeO₂ nanoparticles on the peroxymonosulfate activation in the water, *Environ. Sci. Technol.* 53 (2019) 4500–4510, <https://doi.org/10.1021/acs.est.9b00658>.
- [5] Z.-Y. Guo, C.-X. Li, M. Gao, X. Han, Y.-J. Zhang, W.-J. Zhang, W.-W. Li, Mn–O covalency governs the intrinsic activity of Co–Mn spinel oxides for boosted peroxymonosulfate activation, *Angew. Chem. Int. Ed.* 60 (2021) 274–280, <https://doi.org/10.1002/anie.202010828>.
- [6] C. Gao, Y. Su, X. Quan, V.K. Sharma, S. Chen, H. Yu, Y. Zhang, J. Niu, Electronic modulation of iron-bearing heterogeneous catalysts to accelerate Fe(III)/Fe(II) redox cycle for highly efficient Fenton-like catalysis, *Appl. Catal. B Environ.* 276 (2020), <https://doi.org/10.1016/j.apcatb.2020.119016>.
- [7] J. Lu, C. Chen, M. Qian, P. Xiao, P. Ge, C. Shen, X.L. Wu, J. Chen, Hollow-structured amorphous prussian blue decorated on graphitic carbon nitride for photo-assisted activation of peroxymonosulfate, *J. Colloid Interface Sci.* 603 (2021) 856–863, <https://doi.org/10.1016/j.jcis.2021.06.159>.
- [8] H. Dong, Q. Xu, L. Lian, Y. Li, S. Wang, C. Li, X. Guan, Degradation of organic contaminants in the Fe(II)/peroxymonosulfate process under acidic conditions: the overlooked rapid oxidation stage, *Environ. Sci. Technol.* 55 (2021) 15390–15399, <https://doi.org/10.1021/acs.est.1c04563>.
- [9] D. Wang, L. Zhao, D. Wang, L. Yan, C. Jing, H. Zhang, L.H. Guo, N. Tang, Direct evidence for surface long-lived superoxide radicals photo-generated in TiO₂ and other metal oxide suspensions, *Phys. Chem. Chem. Phys.* 20 (2018) 18978–18985, <https://doi.org/10.1039/c8cp03081b>.
- [10] J. Lee, U. von Gunten, J.-H. Kim, Persulfate-based advanced oxidation: critical assessment of opportunities and roadblocks, *Environ. Sci. Technol.* 54 (2020) 3064–3081, <https://doi.org/10.1021/acs.est.9b07082>.
- [11] S. Liu, Y. Hu, H. Xu, Z. Lou, J. Chen, C.-Z. Yuan, X. Lv, X. Duan, S. Wang, X.-L. Wu, Directional electron transfer in single-atom cobalt nanzyme for enhanced photo-Fenton-like reaction, *Appl. Catal. B Environ.* (2023), <https://doi.org/10.1016/j.apcatb.2023.122882>.
- [12] F. Liu, J. Cao, Z. Yang, W. Xiong, Z. Xu, P. Song, M. Jia, S. Sun, Y. Zhang, X. Zhong, Heterogeneous activation of peroxymonosulfate by cobalt-doped MIL-53(Al) for efficient tetracycline degradation in water: coexistence of radical and non-radical reactions, *J. Colloid Interface Sci.* 581 (2021) 195–204, <https://doi.org/10.1016/j.jcis.2020.07.100>.
- [13] F. Chen, X.-L. Wu, L. Yang, C. Chen, H. Lin, J. Chen, Efficient degradation and mineralization of antibiotics via heterogeneous activation of peroxymonosulfate by using graphene supported single-atom Cu catalyst, *Chem. Eng. J.* 394 (2020), <https://doi.org/10.1016/j.cej.2020.124904>.
- [14] C. Song, Q. Zhan, F. Liu, C. Wang, H. Li, X. Wang, X. Guo, Y. Cheng, W. Sun, L. Wang, J. Qian, B. Pan, Overturned loading of inert CeO₂ to active Co₃O₄ for unusually improved catalytic activity in fenton-like reactions, *Angew. Chem. Int. Ed.* 61 (2022), e202200406, <https://doi.org/10.1002/anie.202200406>.
- [15] M. Qian, X.-L. Wu, M. Lu, L. Huang, W. Li, H. Lin, J. Chen, S. Wang, X. Duan, Modulation of charge trapping by island-like single-atom cobalt catalyst for enhanced photo-fenton-like reaction, *Adv. Funct. Mater.* 33 (2023), <https://doi.org/10.1002/adfm.202208688>.
- [16] X.-L. Wu, S. Liu, M. Yan, H. Lin, J. Chen, S. Liu, S. Wang, X. Duan, Directional and ultrafast charge transfer in oxygen-vacancy-rich ZnO@single-atom cobalt core-

- shell junction for photo-fenton-like reaction, *Angew. Chem. Int. Ed.* (2023), e202305639, <https://doi.org/10.1002/anie.202305639>.
- [17] S. Liu, D. Liu, Y. Sun, P. Xiao, H. Lin, J. Chen, X.-L. Wu, X. Duan, S. Wang, Enzyme-mimicking single-atom FeN₄ sites for enhanced photo-Fenton-like reactions, *Appl. Catal. B Environ.* 310 (2022), <https://doi.org/10.1016/j.apcatb.2022.121327>.
- [18] G. Vilé, P. Sharma, M. Nachtegaal, F. Tollini, D. Moscatelli, A. Sroka-Bartnicka, O. Tomanec, M. Petr, J. Filip, I.S. Pieta, R. Zboril, M.B. Gawande, An earth-abundant Ni-based single-atom catalyst for selective photodegradation of pollutants, *Sol. RRL* 5 (2021), 2100176, <https://doi.org/10.1002/solr.202100176>.
- [19] J. Liu, Y. Zou, D. Cruz, A. Savateev, M. Antonietti, G. Vilé, Ligand–metal charge transfer induced via adjustment of textural properties controls the performance of single-atom catalysts during photocatalytic degradation, *ACS Appl. Mater. Inter.* 13 (2021) 25858–25867, <https://doi.org/10.1021/acsami.1c02243>.
- [20] V. Ruta, A. Sivo, L. Bonetti, M.A. Bajada, G. Vilé, Structural effects of metal single-atom catalysts for enhanced photocatalytic degradation of gemfibrozil, *ACS Appl. Nano Mater.* 5 (2022) 14520–14528, <https://doi.org/10.1021/acsnano.2c02859>.
- [21] C. Wang, J. Gao, C. Gu, Rapid destruction of tetrabromobisphenol A by Iron(III)-tetraamidomacrocyclic ligand/layered double hydroxide composite/H₂O₂ system, *Environ. Sci. Technol.* 51 (2017) 488–496, <https://doi.org/10.1021/acs.est.6b04294>.
- [22] X. Wu, X. Tan, S. Yang, T. Wen, H. Guo, X. Wang, A. Xu, Coexistence of adsorption and coagulation processes of both arsenate and NOM from contaminated groundwater by nanocrystallized Mg/Al layered double hydroxides, *Water Res.* 47 (2013) 4159–4168, <https://doi.org/10.1016/j.watres.2012.11.056>.
- [23] A. Jawad, J. Lang, Z. Liao, A. Khan, J. Ifthikar, Z. Lv, S. Long, Z. Chen, Z. Chen, Activation of persulfate by CuOx@Co-LDH: a novel heterogeneous system for contaminant degradation with broad pH window and controlled leaching, *Chem. Eng. J.* 335 (2018) 548–559, <https://doi.org/10.1016/j.cej.2017.10.097>.
- [24] P. Li, M. Wang, X. Duan, L. Zheng, X. Cheng, Y. Zhang, Y. Kuang, Y. Li, Q. Ma, Z. Feng, W. Liu, X. Sun, Boosting oxygen evolution of single-atomic ruthenium through electronic coupling with cobalt-iron layered double hydroxides, *Nat. Commun.* 10 (2019) 1711, <https://doi.org/10.1038/s41467-019-09666-0>.
- [25] J. Miao, W. Geng, P.J.J. Alvarez, M. Long, 2D N-doped porous carbon derived from polydopamine-coated graphitic carbon nitride for efficient nonradical activation of peroxymonosulfate, *Environ. Sci. Technol.* 54 (2020) 8473–8481, <https://doi.org/10.1021/acs.est.0c03207>.
- [26] Y. Lin, M. Zhou, X. Tai, H. Li, X. Han, J. Yu, Analytical transmission electron microscopy for emerging advanced materials, *Matter* 4 (2021) 2309–2339, <https://doi.org/10.1016/j.matt.2021.05.005>.
- [27] X. Wang, Z. Li, J. Zhang, H. Yan, C. Wang, F. Wu, A. Tian, X. Hong, W. Dong, S. Yang, Effect of average interlayer spacing on capacitance of NiMn layered double hydroxide, *Chem. Eng. J.* 398 (2020), 125618, <https://doi.org/10.1016/j.cej.2020.125618>.
- [28] Y. Hong, J. Peng, X. Zhao, Y. Yan, B. Lai, G. Yao, Efficient degradation of atrazine by CoMgAl layered double oxides catalyzed peroxymonosulfate: optimization, degradation pathways and mechanism, *Chem. Eng. J.* 370 (2019) 354–363, <https://doi.org/10.1016/j.cej.2019.03.127>.
- [29] L. Chen, D. Ding, C. Liu, H. Cai, Y. Qu, S. Yang, Y. Gao, T. Cai, Degradation of norfloxacin by CoFe₂O₄-GO composite coupled with peroxymonosulfate: a comparative study and mechanistic consideration, *Chem. Eng. J.* 334 (2018) 273–284, <https://doi.org/10.1016/j.cej.2017.10.040>.
- [30] R. Ma, X. Cui, Y. Wang, Z. Xiao, R. Luo, L. Gao, Z. Wei, Y. Yang, Pyrolysis-free synthesis of single-atom cobalt catalysts for efficient oxygen reduction, *J. Mater. Chem. A* 10 (2022) 5918–5924, <https://doi.org/10.1039/dta08412g>.
- [31] P. Yu, L. Wang, F. Sun, Y. Xie, X. Liu, J. Ma, X. Wang, C. Tian, J. Li, H. Fu, Co nanoislands rooted on Co-N-C nanosheets as efficient oxygen electrocatalyst for Zn-air batteries, *Adv. Mater.* 31 (2019), e1901666, <https://doi.org/10.1002/adma.201901666>.
- [32] Y. Pan, R. Lin, Y. Chen, S. Liu, W. Zhu, X. Cao, W. Chen, K. Wu, W.C. Cheong, Y. Wang, L. Zheng, J. Luo, Y. Lin, Y. Liu, C. Liu, J. Li, Q. Lu, X. Chen, D. Wang, Q. Peng, C. Chen, Y. Li, Design of single-atom Co-N₄ catalytic site: a robust electrocatalyst for CO₂ reduction with nearly 100% CO selectivity and remarkable stability, *J. Am. Chem. Soc.* 140 (2018) 4218–4221, <https://doi.org/10.1021/jacs.8b00814>.
- [33] P. Wang, Y. Ren, R. Wang, P. Zhang, M. Ding, C. Li, D. Zhao, Z. Qian, Z. Zhang, L. Zhang, L. Yin, Atomically dispersed cobalt catalyst anchored on nitrogen-doped carbon nanosheets for lithium-oxygen batteries, *Nat. Commun.* 11 (2020) 1576, <https://doi.org/10.1038/s41467-020-15416-4>.
- [34] Y. Zhu, W. Sun, J. Luo, W. Chen, T. Cao, L. Zheng, J. Dong, J. Zhang, M. Zhang, Y. Han, C. Chen, Q. Peng, D. Wang, Y. Li, A cocoon silk chemistry strategy to ultrathin N-doped carbon nanosheet with metal single-site catalysts, *Nat. Commun.* 9 (2018) 3861, <https://doi.org/10.1038/s41467-018-06296-w>.
- [35] F. Chen, X.L. Wu, C. Shi, H. Lin, J. Chen, Y. Shi, S. Wang, X. Duan, Molecular engineering toward pyrrolic N-Rich M-N₄ (M = Cr, Mn, Fe, Co, Cu) single-atom sites for enhanced heterogeneous fenton-like reaction, *Adv. Funct. Mater.* 31 (2021), <https://doi.org/10.1002/adfm.202007877>.
- [36] A.M. Dietrich, G.A. Burlingame, Critical review and rethinking of USEPA secondary standards for maintaining organoleptic quality of drinking water, *Environ. Sci. Technol.* 49 (2015) 708–720, <https://doi.org/10.1021/es504403t>.
- [37] K. Qian, H. Chen, W. Li, Z. Ao, Y.N. Wu, X. Guan, Single-atom Fe catalyst outperforms its homogeneous counterpart for activating peroxymonosulfate to achieve effective degradation of organic contaminants, *Environ. Sci. Technol.* 55 (2021) 7034–7043, <https://doi.org/10.1021/acs.est.0c08805>.
- [38] G. Vilé, Photocatalytic materials and light-driven continuous processes to remove emerging pharmaceutical pollutants from water and selectively close the carbon cycle, *Cata. Sci. Technol.* 11 (2021) 43–61, <https://doi.org/10.1039/D0CY01713B>.
- [39] L. Wu, Z. Sun, Y. Zhen, S. Zhu, C. Yang, J. Lu, Y. Tian, D. Zhong, J. Ma, Oxygen vacancy-induced nonradical degradation of organics: critical trigger of oxygen (O₂) in the Fe-Co LDH/peroxymonosulfate system, *Environ. Sci. Technol.* 55 (2021) 15400–15411, <https://doi.org/10.1021/acs.est.1c04600>.
- [40] Z.Y. Guo, Y. Si, W.Q. Xia, F. Wang, H.Q. Liu, C. Yang, W.J. Zhang, W.W. Li, Electron delocalization triggers nonradical Fenton-like catalysis over spinel oxides, *Proc. Natl. Acad. Sci. U. S. A.* 119 (2022), e2201607119, <https://doi.org/10.1073/pnas.2201607119>.
- [41] Y. Feng, P.H. Lee, D. Wu, K. Shih, Surface-bound sulfate radical-dominated degradation of 1,4-dioxane by alumina-supported palladium (Pd/Al₂O₃) catalyzed peroxymonosulfate, *Water Res.* 120 (2017) 12–21, <https://doi.org/10.1016/j.watres.2017.04.070>.
- [42] N. Chen, G. Fang, C. Zhu, S. Wu, G. Liu, D.D. Dionysiou, X. Wang, J. Gao, D. Zhou, Surface-bound radical control rapid organic contaminant degradation through peroxymonosulfate activation by reduced Fe-bearing smectite clays, *J. Hazard. Mater.* 389 (2020), 121819, <https://doi.org/10.1016/j.jhazmat.2019.121819>.
- [43] H. Song, R. Du, Y. Wang, D. Zu, R. Zhou, Y. Cai, F. Wang, Z. Li, Y. Shen, C. Li, Anchoring single atom cobalt on two-dimensional MXene for activation of peroxymonosulfate, *Appl. Catal. B Environ.* 286 (2021), <https://doi.org/10.1016/j.apcatb.2021.119898>.
- [44] W. Ren, G. Nie, P. Zhou, H. Zhang, X. Duan, S. Wang, The intrinsic nature of persulfate activation and N-doping in carbocatalysis, *Environ. Sci. Technol.* 54 (2020) 6438–6447, <https://doi.org/10.1021/acs.est.0c01161>.
- [45] Y. Zhao, L. Yu, C. Song, Z. Chen, F. Meng, M. Song, Selective Degradation of Electron-Rich Organic Pollutants Induced by CuO@Biochar: The Key Role of Outer-Sphere Interaction and Singlet Oxygen, *Environ. Sci. Technol.* 56 (2022) 10710–10720, <https://doi.org/10.1021/acs.est.2c01759>.
- [46] X. Sun, Z. Liu, H. Yu, Z. Zheng, D. Zeng, Facile synthesis of BiFeO₃ nanoparticles by modified microwave-assisted hydrothermal method as visible light driven photocatalysts, *Mater. Lett.* 219 (2018) 225–228, <https://doi.org/10.1016/j.matlet.2018.02.052>.
- [47] I. Berruti, M. Inmaculada Polo-López, I. Oller, J. Flores, M. Luisa Marin, F. Bosca, Sulfate radical anion: Laser flash photolysis study and application in water disinfection and decontamination, *Appl. Catal. B Environ.* 315 (2022), 121519, <https://doi.org/10.1016/j.apcatb.2022.121519>.
- [48] J. Xie, C. Yang, X. Li, S. Wu, Y. Lin, Generation and engineering applications of sulfate radicals in environmental remediation, *Chemosphere* 339 (2023), 139659, <https://doi.org/10.1016/j.chemosphere.2023.139659>.
- [49] H. Shao, J. Chen, J. Xu, Y. Liu, H. Dong, J. Qiao, X. Guan, Naproxen as a turn-on chemiluminescent probe for real-time quantification of sulfate radicals, *Environ. Sci. Technol.* 57 (2023) 8818–8827, <https://doi.org/10.1021/acs.est.3c01948>.